

Article

Estimation of Supraglacial Dust and Debris Geochemical Composition via Satellite Reflectance and Emissivity

Kimberly Casey ^{1,*} and Andreas Kääb ²

¹ Cryospheric Sciences Laboratory, NASA Goddard Space Flight Center, Code 615, Greenbelt, MD 20771, USA

² Department of Geosciences, University of Oslo, 0316 Oslo, Norway;
E-Mail: andreas.kaab@geo.uio.no

* Author to whom correspondence should be addressed; E-Mail: kimberly.a.casey@nasa.gov;
Tel.: +1-301-614-6098; Fax: +1-301-614-5644.

Received: 1 June 2012; in revised form: 31 August 2012 / Accepted: 3 September 2012 /

Published: 7 September 2012

Abstract: We demonstrate spectral estimation of supraglacial dust, debris, ash and tephra geochemical composition from glaciers and ice fields in Iceland, Nepal, New Zealand and Switzerland. Surface glacier material was collected and analyzed via X-ray fluorescence spectroscopy (XRF) and X-ray diffraction (XRD) for geochemical composition and mineralogy. *In situ* data was used as ground truth for comparison with satellite derived geochemical results. Supraglacial debris spectral response patterns and emissivity-derived silica weight percent are presented. Qualitative spectral response patterns agreed well with XRF elemental abundances. Quantitative emissivity estimates of supraglacial SiO₂ in continental areas were 67% (Switzerland) and 68% (Nepal), while volcanic supraglacial SiO₂ averages were 58% (Iceland) and 56% (New Zealand), yielding general agreement. Ablation season supraglacial temperature variation due to differing dust and debris type and coverage was also investigated, with surface debris temperatures ranging from 5.9 to 26.6 °C in the study regions. Applications of the supraglacial geochemical reflective and emissive characterization methods include glacier areal extent mapping, debris source identification, glacier kinematics and glacier energy balance considerations.

Keywords: glaciology; remote sensing; supraglacial dust; tephra; reflectance; ASTER; MODIS; Hyperion

1. Context

Glaciers, icecaps and ice sheets have melted at unprecedented rates over recent decades in response to Earth's changing climate [1,2]. A driving factor influencing this melt is dust and debris cover on land ice surfaces [3–6]. Emerging research suggests global dust and soot flux may have considerably larger impact on glacier melt than currently understood [7–10]. Volcanic eruptions, such as New Zealand's Mt. Ruapehu eruption in September 2007, and Iceland's Eyjafjallajökull eruption in April 2010 and Grimsvötn eruption in May 2011 also result in considerable deposition of ash and tephra on ice caps and glaciers. Long-range atmospheric transport of particulates [11–13], changes in regional land use [14], recession of ice and atmospheric re-emission of fine grained silt [15] and regional rockfall and sediment re-emission are the primary factors contributing to glacier surface particulate composition. The geochemical composition of surface glacier debris can indicate provenance—whether debris is locally attributed or transported to the glacier. Further, the composition and extent of glacier surface particulates influences albedo and the amount of solar radiation absorbed at the ice surface.

Satellite estimation of surface glacier geochemical composition is a new field of research (e.g., [16]) and can be used to quantify glacier surface compositions on large spatial and temporal scales. Such glacio-geochemical mapping methods allow for monitoring changing patterns in debris cover and composition over seasonal, annual or multi-year time periods. Techniques discussed in this study could be included in larger regional (e.g., [17–19]) or global (e.g., [20,21]) glacier monitoring inventories.

We study four distinct continental and volcanic glacier regions to demonstrate supraglacial geochemical mapping capabilities. Field collected supraglacial debris samples were measured for mineral and elemental composition via X-ray diffraction (XRD) and X-ray fluorescence spectroscopy (XRF), respectively. Field collected surface glacier debris serve as ground truth for comparison with satellite reflectance and emissivity geochemical estimations. Supraglacial dust and debris geochemical compositions are estimated by reflectance response patterns and emissivity-based silica (SiO_2) weight percent estimates. Emissivity derived glacier surface temperatures are measured over varying debris coverage, to explore influences on surface temperature due to surface glacier dust and debris coverage.

2. Study Areas

Our spectral geochemical estimation method is applied to glaciers in near Arctic and mid-latitude, northern and southern hemisphere, volcanically and land-dust influenced areas in Switzerland, Nepal, Iceland and New Zealand (Figure 1). The differing geologic settings, climate, and glacial types (e.g., temperate, summer accumulation type, ice cap, alpine valley glacier, cirque) offer distinct supraglacial dust and debris composition types (Table 1).

The Western Swiss Alps geologic composition is based upon Apulian/African continental plate convergence, resulting in Jurassic ophiolites and associated oceanic metasediments, Cretaceous calcschists and shales, as well as Protero-Paleozoic granites and gneisses [22]. Three glaciers near the Matterhorn (4,478 m) were studied: Findelen, Gorner and Zmutt. Glacier elevations span from 2,240 to 4,450 m, and the three glaciers offer a unique set of neighboring valley glaciers with different types and spatial distributions of supraglacial debris. Findelen is dust covered in the ablation zone, considered by the World Glacier Monitoring Service as a characteristic valley glacier and has been studied over a

century (e.g., [23,24]). Gorner contains medial and lateral debris bands as well as englacial transport of cold (*i.e.*, below freezing) ice from accumulation zone to re-emergence in the ablation zone resulting in intricate winding melt water channels of cold (rather than temperate) bare ice framed by debris bands. The third Swiss Alps study glacier, Zmutt, is heavily debris covered in the ablation zone. Three distinct longitudinal debris bands flow down Zmutt, resulting from lateral geologic differences and weathering factors (for description of geochemical weathering in region, see [25]). An iron-rich coating is present on the northern supraglacial longitudinal longitudinal debris band and can be visually contrasted from the non-weathered debris on the southern side and granitic central Zmutt debris (Figure 2).

Figure 1. Map of study region locations, indicated by the cyan boxes.

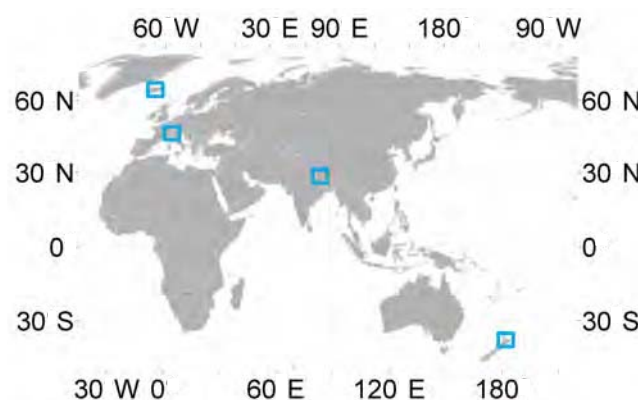


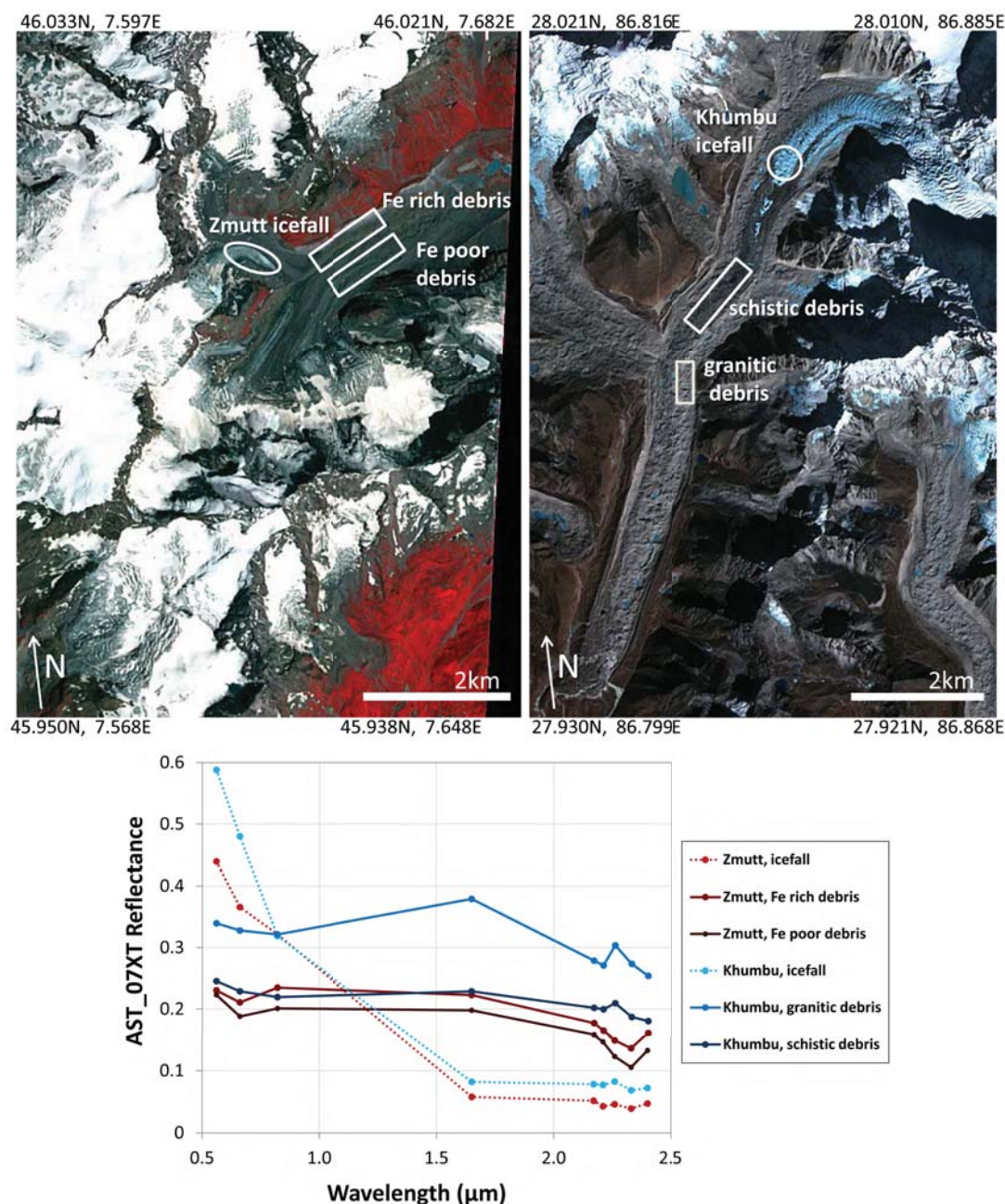
Table 1. Characteristics of glacier study regions. (Swiss climate data from MeteoSwiss and [26], elevations from Swisstopo, 2004; Nepal climate data from [27], elevations from [28]; Iceland climate data from [29], elevations from [30]; New Zealand climate data from New Zealand National Institute of Water and Atmospheric Research, Whakapapa Village (1100 m). Elevations from New Zealand Department of Conservation, 2004.)

Study Region, Glacier (Latitude, Longitude)	Glacier Type, Influences	Mean Annual Temp., Precipitation Elevation (m.a.s.l.)
Zermatt Area, Switzerland (46.00 N 7.65 E)	Mid-latitude, valley glaciers dust and debris covered	3.5 °C, 700 mm 2,240–4,450 m
Khumbu, Ngozumpa, Nepal (27.98 N 86.84 E)	Debris covered continental valley glaciers. Temperate, summer accumulation	−2.4 °C, 470 mm 4,900–8,848 m
central ice caps, Iceland (64.30 N, 18.05 W)	Near-Arctic, maritime ice caps, volcanic influences	−0.4°C, 740 mm 0–2,100 m
Mt. Ruapehu area, New Zealand (39.27 S 175.56 E)	Cirque glaciers, volcanic influences	6.1 °C, 1,100 mm 2,200–2,797 m

The Himalayan mountain range is formed by the convergence of the Eurasian and Indian tectonic plates, and extends from the Karakoram and Hindu Kush in the northwest to the Khumbu, Lhasa and Bhutanese region in the southeast. The southeastern Nepal Khumbu Himalaya area geologically consists of mid- and early Tertiary leucogranites, gneisses, and shales [31]. The glaciers in the Khumbu Himalaya region, including Imja, Khumbu, Lhotse Shar and Ngozumpa glaciers, are heavily debris covered in the

ablation zone [32]. Of the contrasting geographic areas in this study, the Khumbu Himalaya glaciers are closest to the equator, highest in elevation—Ngozumpa glacier spans from *ca.* 8,188 m to 4,700 m and Khumbu glacier spans from 8,848 m (the highest point on Earth) to 4,900 m [28], and contain the most extensive debris cover. Atmospheric deposit from local continental dust influences area glaciers [33], yet the majority of glacial debris is due to frequent rock and ice avalanches from surrounding extreme terrain [28].

Figure 2. ASTER (band 3,2,1) images of Zmutt glacier (top left, acquired 29 July 2004) and Khumbu glacier (top right, acquired 29 November 2005). VNIR-SWIR multispectral AST_07XT reflectance is plotted beneath the images. Zmutt glacier serpentine Fe rich and Fe poor longitudinal debris bands can be differentiated from the Khumbu glacier leucogranite lighter granitic and darker schistic longitudinal debris bands.



The near Arctic Iceland ice caps span in elevation from sea level to 2,100 m and are located on some of the youngest bedrock on Earth. Bisected by the Mid-Atlantic Ridge from north to south, the center of Iceland where Hofsjökull and Mýradalsjökull are located consists of Holocene sediment. Vatnajökull, the largest ice cap in Iceland (and Europe), covers approximately 8,000 km² [34] extending from the center of the island to near the eastern Icelandic coast, straddling Holocene sediment, and earlier Quaternary and Tertiary bedrock moving from west to east [35]. Hofsjökull, Mýradalsjökull and Vatnajökull ice caps are influenced by high volcanic activity, with over 205 Icelandic eruptive events recorded [36]. Tephra deposition and re-emission dominates surface dust and debris on Iceland's ice caps (tephrachronology further discussed in [37]). Of particular interest to this study is the recent April 2010 Eyjafjallajökull eruption, subsequent basaltic tephra deposition and ablation season of 2010. The heaviest tephra deposition resulting from the April 2010 Eyjafjallajökull eruption was on Mýradalsjökull, followed by Vatnajökull and Hofsjökull.

Located mid-latitude in the southern hemisphere, bordered by the Pacific Ocean to the north and east and the Tasman sea to the west, the north island of New Zealand is typified by a temperate climate with prevailing westerly winds. Eight small cirque glaciers lie about the summit of the active Quaternary andesitic stratovolcano Mt. Ruapehu (2,797 m, the highest peak on the north island) [38,39]. Mt. Ruapehu glacier elevations span from 2,200 to 2,797 m, and experience high precipitation, with seasonal snow cover [40,41]. The warm acidic Crater Lake at the summit (typically between 15 and 40 °C) provides a continual sulfur and to a lesser extent chloride and magnesium aerosol influence on Mt. Ruapehu glaciers [42,43]. Mt. Ruapehu glaciers are also affected by the frequent volcanic eruptions, which are predominantly steam, periodically magmatic, and occasionally lahars—in all, over 60 such events are documented since 1945 [44–46]. The last large Mt. Ruapehu eruption occurred on 25 September 2007 (discussed in [47,48]) and the ablation season following the 2007 eruption is analyzed in this study. From the frequent volcanic eruptions, tephra layers in glacier ice are numerous and can be up to 0.5 m thick, consisting of fine ash to ballistics, with plagioclase, pyroxene, elemental sulfur, anhydrite, pyrite, and alunite dominant mineralogy [44,48]. Thin tephra layers on Mt. Ruapehu have been shown to enhance glacier melt; thicker tephra layers have resulted in sub-tephra melting and creation of ice dolines [49].

3. Data Collection and Methods

3.1. Field Sampling and Geochemical Analysis

A total of 54 supraglacial debris samples were collected as follows: 30 debris samples from Findelen and Zmutt glaciers in Valais, Switzerland in September and October 2010; 22 debris samples from Ngozumpa and Khumbu glaciers in Nepal in November 2009 and December 2009 and 2 debris samples from Mangatoetoeu glacier in New Zealand in March 2010. Supraglacial debris samples were collected in clean polyethylene bags, obtaining at least 100 g of debris per sample, and double bagged for transport. All in situ samples were taken in duplicate. Field sample geographic position, elevation and geologic type are detailed in Table 2.

Supraglacial debris samples were analyzed for mineralogy via X-ray diffraction (XRD) and geochemical composition via X-ray fluorescence spectrometry (XRF) at the University of Oslo, Department of Geosciences. To prepare for this analysis, debris samples were oven dried 2 days at 80 °C and crushed to a fine powder (less than 125 μm particle size) via a vibratory ringmill. The fine powder was then prepared into XRD measurement discs and XRF sample tablets for measurement—further detailed in [50]. Note, mineralogy and geochemical composition of Eyjafjallajökull tephra is taken from [51] “explosive ash” as field samples were not collected in this region. For the purposes of this study, geochemical compositions are summarized as supraglacial debris sample averages of the dominant minerals and bulk oxides (with particular inclusion of spectrally influential oxides, e.g., MnO and Fe_2O_3) at the target glaciers (Table 3).

Table 2. Surface glacier debris sample attributes, including location, elevation, collection date.

Location	Date	Latitude/Longitude	Elevation (m a.s.l.)	Debris type
Mid-Findelen	3 October 2010	46.0108°N 7.8267°E	2,675	silt, gravel, rock
Lower Findelen	29 September 2010	46.0109°N 7.8237°E	2,590	silt, gravel, rock
Northern Zmutt	2 October 2010	46.0023°N 7.6528°E	2,345	gravel, rock
Mid-Zmutt	7 October 2010	46.0026°N 7.6560°E	2,255	silt, gravel, rock
Southern Zmutt	7 October 2010	45.9989°N 7.6560°E	2,279	rock
Upper Ngozumpa	27 November 2009	27.9568°N 86.6980°E	4,760	silt, sand, gravel, rock
Mid-Ngozumpa	29 November 2009	27.9537°N 86.6992°E	4,750	gravel, rock
Lower Ngozumpa	26 November 2009	27.9511°N 86.7020°E	4,790	soil, gravel
Upper Khumbu	6 December 2009	27.9998°N 86.8511°E	5,280	gravel
Mid-Khumbu	5 December 2009	27.9874°N 86.8405°E	5,180	sand, rock
Lower Khumbu	4 December 2009	27.9763°N 86.8304°E	5,100	silt, rock
Eyjafjallajökull	15 April 2010	55 km east of crater	100	ash
Mangatoetoenui	5 March 2010	39.275°S 175.590°E	2,450	fine and gravel sized tephra

Table 3. X-ray diffraction determined mineralogy and X-ray fluorescence spectrometry determined weight percent bulk oxides of supraglacial debris from the four study regions.

Region, Glacier	Principal Minerals	Na ₂ O	MgO	Al ₂ O ₃	SiO ₂	CaO	MnO	Fe ₂ O ₃
Switzerland								
Findelen (n=9)	quartz, amphibole, plagioclase	2.42	8.10	13.70	54.34	5.11	0.13	7.82
Zmutt (n=15)	quartz, plagioclase, serpentine	2.5	5.96	13.65	53.91	5.92	0.10	5.96
Nepal								
Khumbu (n=14)	feldspar, mica, quartz	2.60	1.76	13.68	60.76	5.82	0.08	4.43
Ngozumpa (n=8)	quartz, feldspar, mica	2.64	1.30	11.93	56.05	10.67	0.07	3.48
Iceland								
Eyjafjallajökull [after 51]	cristobalite, anorthite, pyroxene	5.01	2.3	14.87	57.98	5.5	0.24	(FeO 9.75)
New Zealand								
Mangatoetoenui (n=2)	plagioclase, pyroxene	2.89	4.23	15.00	55.54	7.07	0.12	7.69

3.2. Spectral Satellite Data and Analysis

We apply the reflectance and emissivity earth observation methods widely used in geologic studies [52,53] toward specifying mineral and geochemical composition of supraglacial dust and debris.

Earth observing sensors with moderate to fine spatial and spectral resolution are most suitable to supraglacial debris mapping. NASA Earth Observing System sensors ALI, ASTER, Hyperion, Landsat and MODIS are used in this study (further sensor details at <http://www.nasa.gov/missions/current/> under Earth Observing-1, Terra and Landsat) due to the free, readily available, long temporal data record. The large spatial, frequent temporal and high spectral resolution provided by MODIS allows reflectance analysis over ice caps and ice sheets (e.g., [54]). The finer spatial resolution of ALI (10 m panchromatic, 30 m VNIR-SWIR), ASTER (15 m VNIR, 30 m SWIR, 90 m TIR), Hyperion (30 m VNIR-SWIR) and Landsat (ETM+: 15 m panchromatic, 30 m VNIR-SWIR, 60 m TIR) are amenable to mapping smaller glaciers.

Reflectance supraglacial dust and debris response patterns are measured by the ASTER VNIR and cross talk corrected SWIR AST_07XT surface reflectance product [55], MODIS MOD09GA surface reflectance product, and Hyperion top-of-atmosphere planetary reflectance after [56], with water vapor, oxygen and carbon dioxide atmospheric absorption features removed (listed in [57]). For surface reflectance analysis, ASTER AST_07XT was used in all study regions, MODIS MOD09GA surface reflectance was used in Iceland due to the large spatial extent of the ice caps, and Hyperion top-of-atmosphere reflectance was used in Khumbu Himalaya and Iceland. (At the time of publication, Hyperion data over Swiss Alps study glaciers and ablation season Mt. Ruapehu study glaciers was not available.) MODIS was also particularly useful in the spectral analysis of Iceland ice caps as ASTER data after 2008 lacks SWIR acquisition capability. Both ASTER AST_07XT and MODIS MOD09GA provide atmospherically corrected at-surface reflectance. Hyper- and multispectral satellite sensors, data products and acquisition dates of scenes used for analysis are given in Table 4.

Table 4. Satellite sensors, data products and dates evaluated for each study region.

Study Region	Sensor, Product	Date, Method / Use
Switzerland	ASTER, AST_07XT	29 July 2004, reflectance
	ASTER, AST_05	21 July 2006, TIR SiO ₂
	ASTER, AST_08	7 July 2010, surface temperature
	Landsat TM	1 September 2010, imagery
Nepal	ALI	4 October 2010, imagery
	ASTER, AST_07XT, AST_05, AST_08	29 November 2005, reflectance, TIR SiO ₂ , surface temperature
	Hyperion	13 May 2002, hyperspectral reflectance
Iceland	ASTER, AST_07XT, AST_05, AST_08	25 August 2010, reflectance, TIR SiO ₂ , surface temperature
	Hyperion	24 September 2001, hyperspectral reflectance
	Landsat ETM+	25 August 2010, surface temperature
	MODIS, MOD09GA	28 August 2010, reflectance
New Zealand	ASTER, AST_07XT, AST_05, AST_08	9 January 2008, reflectance, TIR SiO ₂ , surface temperature
	Hyperion	13 September 2009, hyperspectral reflectance

Emissivity supraglacial dust and debris mapping utilized the ASTER AST_05 surface emissivity product to investigate supraglacial debris silica weight percent composition (after [58], detailed in [50]). ASTER AST_05 TIR estimates of silica weight percent were calculated in all regions and compared with field sample XRF geochemical results. To provide a first-order evaluation of surface temperature variability of supraglacial dust and debris composition, the ASTER surface kinetic temperature AST_08 product was used to measure surface glacier temperatures in all regions. Due to the large spatial extent of ice caps in Iceland, and the inability to use MODIS surface temperature due to loss of thermal signal in heavy tephra covered regions in August 2010 data, Landsat ETM+ was used to measure surface temperature in Iceland. To derive supraglacial temperatures from Landsat ETM+, TIR band 6 data was converted to surface temperature after [59], detailed in [60], with use of a “dirty ice” emissivity value of 0.96 from [61]. Supraglacial temperatures were then investigated in each region with respect to the amount of dust and debris cover.

Spaceborne geochemical estimation results were compared with field collected and laboratory analyzed supraglacial debris. This in situ data was used for comparison with satellite estimates. In situ data in this case is used qualitatively for comparisons. In the field, supraglacial debris was sampled from roughly $0.5\text{ m} \times 0.5\text{ m}$ surface areas, while satellite pixels represent 15 m, 30 m (ASTER), 30 m (Hyperion), 250 m, 500 m, 1 km (MODIS). Thus, with the consideration of mixed pixel effects [62], as well as the temporal difference in collection of supraglacial debris and the acquisition of satellite scene, results must be treated qualitatively.

4. Results and Discussion

4.1. Use of Multispectral Reflectance Response Patterns

To determine supraglacial geochemical composition from multispectral data, ice area reflectance responses were measured over varying supraglacial debris types in each of the four glacier study regions. Continental supraglacial debris reflectance response patterns from Switzerland and Nepal are presented in Figure 2, numerical averages listed in Table 5. Swiss Alps, Zmutt supraglacial debris ASTER AST_07XT VNIR-SWIR reflectance response patterns show characteristic Fe absorption in the visible (*i.e.*, a dip in ASTER band 2), due to the serpentine geology, as well as characteristic hydroxide absorption in SWIR ASTER bands 7 and 8 (absorption features discussed in [63]). The non-weathered debris found on the southern side of the Zmutt ablation area display lower overall VNIR-SWIR reflectance than the weathered, Fe-rich supraglacial debris on the northern side of Zmutt glacier. The granitic central longitudinal debris band on Zmutt shows higher SWIR values (central granitic debris not shown in Figure 2). Zmutt icefall reflectance follows the characteristic glacial bare ice high visible reflectance and lower NIR and SWIR reflectance. Yet, even the lightly dust covered ice near the Zmutt icefall displays a similar reflectance response pattern in the SWIR, AST_07XT bands 5–9, specifically with absorption at band 8 (2.295–2.365 μm). All three Zmutt reflectance response patterns from dust to heavier debris-covered ice display the ASTER visible Fe and SWIR OH absorption features. The transition metal (*i.e.*, Cr, Mn, Fe, Ni, Cu) absorption feature plotted in all of the reflectance response

patterns is affirmed by the high MnO and Fe₂O₃ determined by XRF results (Table 3). The magnitude of the reflectance response pattern is indicative of the percent dust and debris coverage of the ice.

Table 5. Visible to shortwave infrared average reflectances of bare, dust and debris covered ice in the four glacier study regions. The ASTER AST_07XT VNIR and Crosstalk Corrected SWIR Surface Reflectance and MODIS MOD09GA Surface Reflectance data products were used for average reflectance calculations. Areas reported and reflectance signatures are visualized in Figures 2 and 3. The number of pixels, spatial resolution and standard deviations for each average reflectance calculation are listed in the row below reflectance measurements.

Region, Date	Glacier	Satellite Reflectance per Spectral Band, (Band median wavelength shown directly below band number (μm))							
		MOD1	MOD2	MOD3	MOD4	MOD5	MOD6	MOD7	
		0.469	0.555	0.645	0.859	1.24	1.64	2.13	
Iceland 28 August 2010	Hofsjökull, less tephra n=35pts @ 500m	0.469 (0.054)	0.499 (0.059)	0.482 (0.057)	0.392 (0.042)	0.055 (0.008)	0.009 (0.003)		
	Vatnajökull, less tephra n=419pts @ 500m	0.380 (0.047)	0.387 (0.050)	0.374 (0.047)	0.319 (0.034)	0.081 (0.053)	0.013 (0.004)	0.005 (0.002)	
	Mýradalsjökull, less tephra n=42pts @ 500m	0.172 (0.013)	0.188 (0.014)	0.193 (0.015)	0.187 (0.015)	0.060 (0.009)	0.013 (0.001)	0.005 (0.002)	
	Mýradalsjökull, heavy tephra n=203pts @ 500m		0.014 (0.005)	0.019 (0.005)	0.023 (0.005)	0.021 (0.024)	0.021 (0.002)	0.017 (0.002)	
		AST1	AST2	AST3	AST4	AST5	AST6	AST7	AST8
		0.56	0.66	0.82	1.65	2.17	2.21	2.26	2.33
Switzerland 29 July 2004	Zmutt, icefall n=65 @ 15m, 16 @ 30m	0.439 (0.087)	0.366 (0.075)	0.321 (0.056)	0.058 (0.006)	0.051 (0.005)	0.042 (0.004)	0.046 (0.003)	0.038 (0.006)
	Zmutt, northern debris n=106 @ 15m, 28 @ 30m	0.230 (0.008)	0.211 (0.011)	0.235 (0.011)	0.223 (0.004)	0.178 (0.004)	0.165 (0.004)	0.149 (0.003)	0.137 (0.003)
	Zmutt, southern debris n=354 @ 15m, 84 @ 30m	0.223 (0.014)	0.188 (0.014)	0.201 (0.011)	0.198 (0.006)	0.158 (0.007)	0.147 (0.006)	0.123 (0.006)	0.106 (0.006)
		AST9							
		0.047 (0.002)							
Nepal 29 November 2005	Khumbu, bare ice n=475 @ 15m, 144 @ 30m	0.588 (0.132)	0.480 (0.103)	0.319 (0.055)	0.082 (0.008)	0.078 (0.008)	0.077 (0.008)	0.082 (0.008)	0.068 (0.008)
	Khumbu, heavy schistic debris n=1052 @ 15m, 270 @ 30m	0.245 (0.038)	0.229 (0.036)	0.219 (0.033)	0.229 (0.028)	0.202 (0.020)	0.200 (0.021)	0.210 (0.022)	0.187 (0.022)
	Khumbu, heavy granitic debris n=652 @ 15m, 165 @ 30m	0.339 (0.061)	0.328 (0.063)	0.321 (0.058)	0.379 (0.053)	0.279 (0.038)	0.271 (0.039)	0.304 (0.041)	0.274 (0.040)
New Zealand 9 January 2008	Mangaehuehu, least tephra n=433 @ 15m, 108 @ 30m	0.793 (0.042)	0.667 (0.038)	0.557 (0.029)	0.049 (0.004)	0.028 (0.014)	0.017 (0.011)	0.015 (0.012)	0.018 (0.010)
	Mangatoetoenui, slight tephra n=419 @ 15m, 104 @ 30m	0.672 (0.058)	0.581 (0.049)	0.511 (0.034)	0.050 (0.004)	0.023 (0.011)	0.016 (0.013)	0.014 (0.009)	0.019 (0.010)
	Whakapapa, heavy tephra n=333 @ 15m, 77 @ 30m	0.178 (0.015)	0.135 (0.013)	0.164 (0.011)	0.106 (0.009)	0.065 (0.015)	0.067 (0.014)	0.063 (0.013)	0.071 (0.014)

Two geochemically distinct areas and the icefall of Khumbu glacier were analyzed via ASTER AST_07XT (Figure 2). The schistic supraglacial debris found in the center of Khumbu glacier shows lower overall VNIR-SWIR reflectance than the lateral granitic supraglacial debris bands. The lateral granitic supraglacial debris displays a characteristic peak in NIR, ASTER band 4, (1.600–1.700 μm)

representative of hydrated silicate abundance. In contrast to the Zmutt reflectance response patterns, both granitic and schistic debris and icefall Khumbu supraglacial reflectance display a peak in ASTER band 7 (2.235–2.285 μm)—suggesting high silicate content and carbonaceous shales. Further, the Khumbu glacier spectral reflectance response patterns display much less of a VNIR absorption feature, suggesting low Fe and Mn content. The geochemical XRF results validate the high amount of silicates and carbonates and low Fe and Mn abundances (Table 3) indicated by the Khumbu glacier VNIR-SWIR reflectance response patterns.

For the reflectance comparison over volcanic supraglacial debris in Iceland, MODIS MOD09GA bands 1–2 (250 m aggregated to 500 m) and bands 3–7 (500 m) were used. The MODIS data was acquired on 28 August 2010 in the ablation season immediately following the spring 2010 Eyjafjallajökull eruptions. Icelandic supraglacial tephra was analyzed at heavily tephra covered Mýradalsjökull, as well as less tephra covered Vatnajökull and even lesser tephra covered ice at Hofsjökull. The heaviest tephra, located on Mýradalsjökull, geographically nearest to the Eyjafjallajökull eruption, was found to correspond with the lowest VNIR-SWIR reflectance of the study region (Figure 3, Table 5). Similarly, the greater the distance from Eyjafjallajökull, the larger the VNIR-SWIR ice reflectance in the August 2010 reflectance data analysis. The highest VNIR-SWIR reflectance response patterns were found at Hofsjökull, with the largest distance from Eyjafjallajökull and probably least amount of supraglacial tephra. (Note, due to cloud cover in the scene, the higher areas of Vatnajökull were not analyzed for reflectance, but likely display similarly high reflectance due to low supraglacial tephra.)

New Zealand Mt. Ruapehu supraglacial reflectance response patterns were assessed over Whakapapa heavily tephra covered glacier, and lesser tephra covered Mangatoetoenui and Mangaehuehu glaciers (Figure 3). The September 2007 Mt. Ruapehu eruption resulted in tephra deposited northward, with heavy deposition on Whakapapa glacier, and the next greatest tephra deposition on Mangatoetoenui glacier. Similar to the Icelandic analysis, the ablation season following eruption is used to analyze debris reflectance patterns (ASTER data acquired 9 January 2008). The further geographic distance from the initial volcanic tephra deposition area, the greater the supraglacial reflectance potential. Increasing tephra coverage on ice decreased VNIR reflectance; for heavily tephra covered ice, VNIR-SWIR reflectance remained well below 0.2. ASTER SWIR bands are nearly featureless in all magnitudes of tephra coverage (*i.e.*, near zero slope of AST.07XT bands 4–9, MODIS bands 5–7). ASTER visible band 2 absorption can be seen in all Mt. Ruapehu glacier reflectance response patterns, with the greatest band 2 absorption seen in the heaviest Whakapapa debris cover, signaling high transition metal (*e.g.*, Fe) content in Mt. Ruapehu eruptive material. The high transition metal concentrations signaled by the reflectance response patterns are also found in the supraglacial samples from Mangatoetoenui glacier (presented in Table 3).

VNIR-SWIR reflectance analysis suggests glacier debris geochemical distinction mapping thresholds. Specifically, supraglacial debris consisting primarily of volcanic tephra may be differentiated by VNIR reflectance below 0.2 and SWIR reflectance below 0.1 even at relatively low tephra concentrations (as shown in Iceland and New Zealand analysis—Figure 3). The higher silica content characteristic of continental-based supraglacial debris may be signaled by reflectance thresholds of VNIR reflectance above 0.2 and SWIR signatures above 0.1, typically well above 0.1 and ranging up to 0.4 (Figure 2).

Increased transition metal (e.g., Fe, Mn) concentrations in all supraglacial debris types were indicated by visible absorption features as shown in the Zmutt glacier debris (Figure 2) and Mt. Ruapehu tephra (Figure 3). Threshold values identified in this study could be explored further and used in glacier dust and debris composition automated or semi-automated algorithms, for example, describing supraglacial compositions on global scales for use in global glacier databases (e.g., GLIMS, WGMS—perhaps relevant to glaciologists conducting global energy balance calculations or creating global inventories of debris variability).

Figure 3. Images of the Iceland study region (top left, MODIS bands 1,4,3, acquired 28 August 2010) and Mt. Ruapehu, New Zealand study region (top right, ASTER bands 3,2,1, acquired 9 January 2008) are shown below. VNIR-SWIR multispectral MOD09GA (Iceland) and AST_07XT (New Zealand) surface reflectance means are plotted beneath the images. Note, the red box on Hofsjökull indicates the coverage of the Hyperion scene, discussed in Section 4.2, Figure 4.

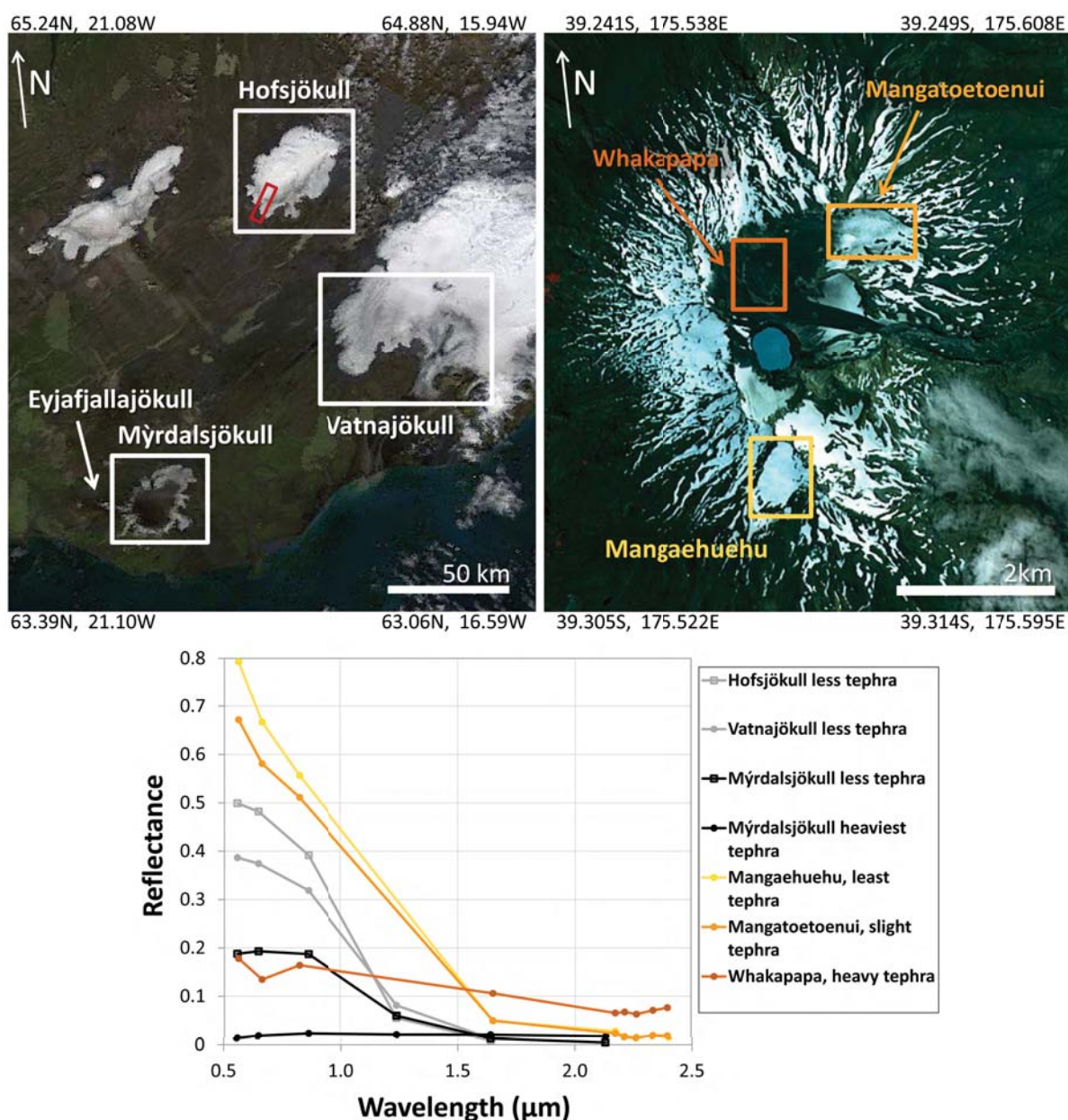
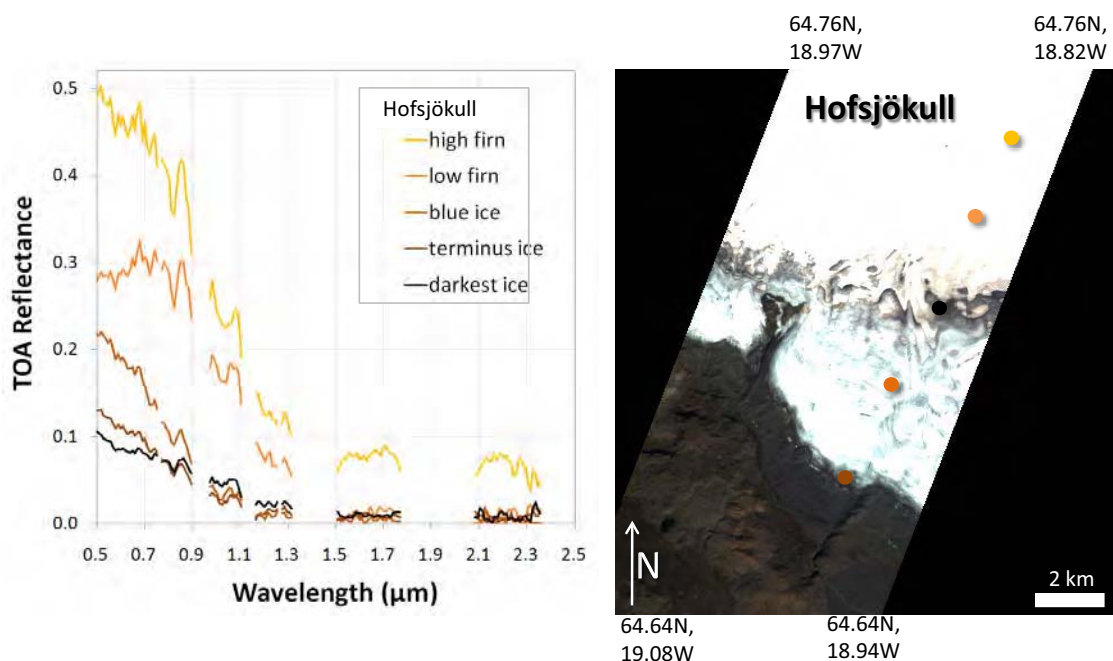


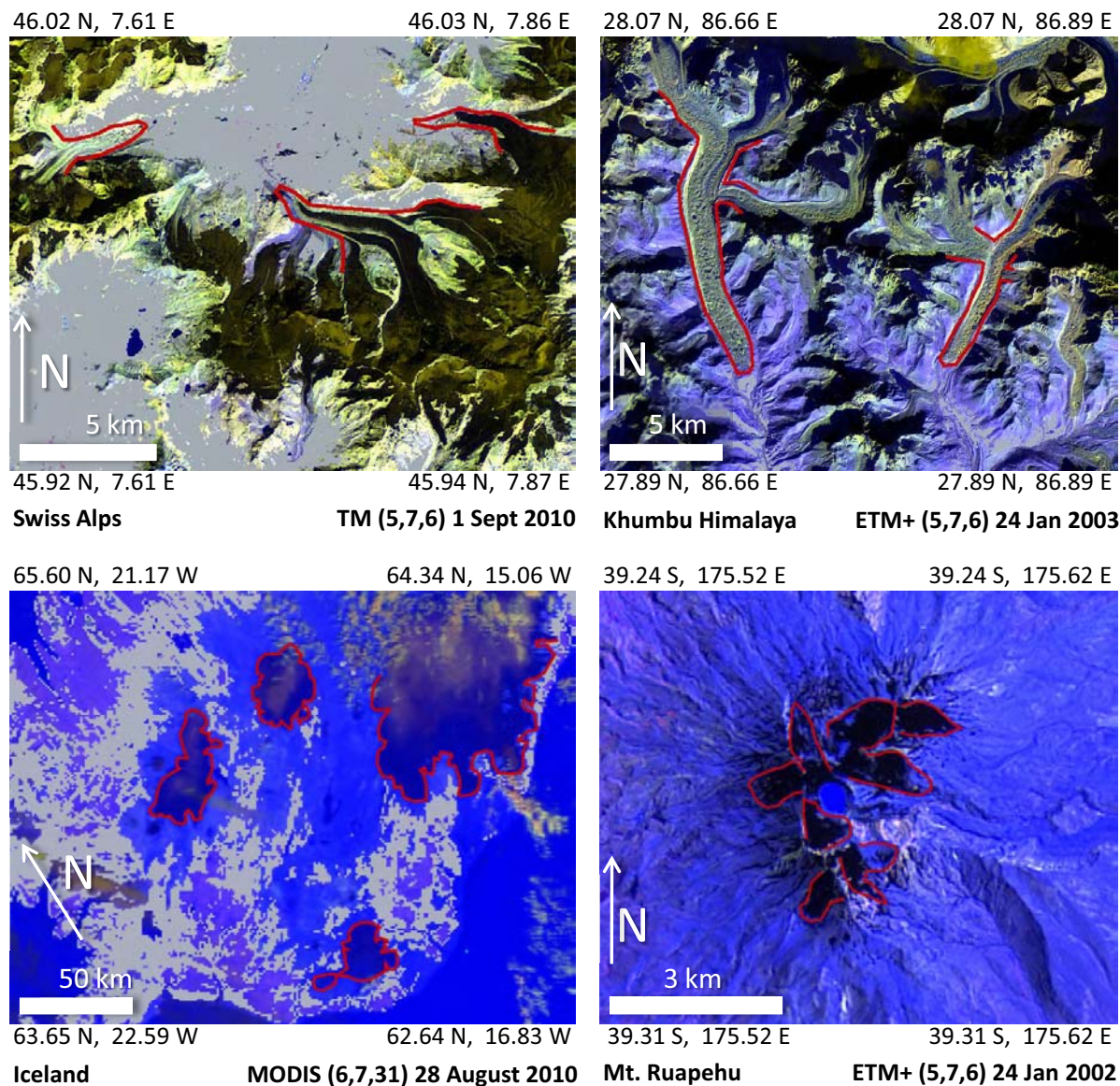
Figure 4. Hofsjökull Hyperion (24 September 2001) at-sensor top-of-atmosphere supraglacial reflectance plotted at left, and the true color image is displayed on the right. Circles on the Hofsjökull image display the areas with varying tephra coverage in which reflectance data was selected to plot. The same colors are used for circles as the top-of-atmosphere reflectance response patterns (e.g., lightest orange indicating high firn, black indicating heaviest tephra covered ice). Atmospheric water vapor, oxygen and CO₂ absorption features are removed.



A simple means to indicate supraglacial volcanic ash and tephra vs. continental dust and debris is use of SWIR and TIR spectral bands to create false color composites [50,64]. Figure 5 displays the relative silica rich supraglacial debris in the continental Swiss Alp and Khumbu Himalaya regions and the silica poor supraglacial debris in the volcanic Iceland and New Zealand study regions. The images above are created from Landsat SWIR, TIR bands 5,7,6 and MODIS 6,7,31 as labeled. Ablation areas of study glaciers are outlined in red and vegetation was filtered out for all scenes using a normalized difference vegetation index mask.

Beyond the scope of this study, but also useful in estimating supraglacial debris geochemistry via multispectral data, include the following methods. SWIR and TIR based band ratios (e.g., [50,65,66]) over supraglacial dust and debris areas can be used to derive semi-quantitative estimates of supraglacial debris mineral abundances. Multispectral data absorption feature location and depth analysis via VNIR-TIR spectral angle relationships (e.g., [67]) is also possible in mapping glacier surface mineralogy. Linear spectral mixture analysis (e.g., [68,69]) could also prove useful in estimating glacier surface compositions.

Figure 5. Shortwave and thermal infrared false color image composites of study regions differentiate silica rich (yellow coloring) vs. silica poor (blue coloring) supraglacial debris mineralogy.

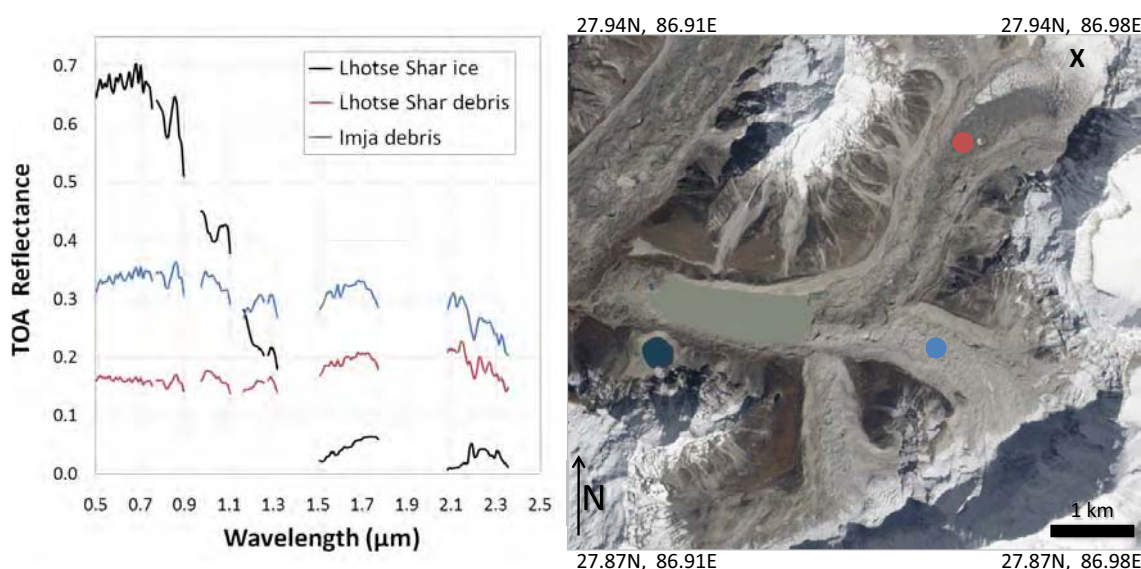


4.2. Use of Hyperspectral Reflectance Response Patterns

The Khumbu Himalaya and Iceland study regions offer continental debris vs. volcanic tephra supraglacial geochemical compositions. Hyperion derived planetary reflectance of two distinct types of continental supraglacial debris from Lhotse Shar and Imja glaciers as well as bare ice from Lhotse Shar glacier is plotted in Figure 6. The hyperspectral data indicates that Lhotse Shar supraglacial debris is likely to be more schistic than the Imja supraglacial debris, which is likely to be more granitic—signaled by the shapes and overall magnitudes of VNIR-SWIR reflectance. Figure 4 shows hyperspectral signatures from Hofsjökull at slight to moderate tephra covered supraglacial areas. Generally, volcanic supraglacial ash and tephra hyperspectral VNIR-SWIR planetary reflectance signatures follow VNIR-SWIR surface reflectance multispectral estimates. Supraglacial tephra found

on Hofsjökull translates to very low, featureless SWIR values and conversely, continental supraglacial debris from Lhotse Shar and Imja glaciers display higher VNIR and SWIR reflectance. Although beyond the scope of this study, with atmospheric correction, Hyperion data are theoretically amenable to supraglacial mineralogic differentiation using continuum removal and/or logical operator techniques for discriminating small-scale wavelength and absorption depth-dependent characteristics of glacier surface particulates [70,71]. Component specific absorption features, for example due to silicate-rich dust vs. calcite-rich dust, could be used to attempt a more quantitative assessment of supraglacial composition.

Figure 6. Lhotse Shar (reflectance data taken at red dot) and Imja glacier (reflectance data taken at blue dot) Hyperion at-sensor top-of-atmosphere reflectance of supraglacial ice and debris, taken from 13 May 2002 Hyperion acquisition. Atmospheric water vapor, oxygen and CO₂ absorption features were removed. The true color image composite is displayed on the right, and was acquired by ALI on 4 October 2010 (10m pan enhanced image shown). The black “X” on upper Lhotse Shar glacier shows the area used for the spectral reflectance data collection.



4.3. Use of Emissivity to Measure Silica Content

In addition to the supraglacial debris composition identified by VNIR-SWIR spectral reflectance, TIR emissivity supraglacial debris silica weight percent abundance allows for an independent estimate of surface glacier debris composition. TIR bands are particularly indicative of carbonate and silicate supraglacial abundances. TIR satellite estimated SiO₂ weight percent was calculated using the ASTER AST_05 Surface Emissivity product (Equation (1) after [58]). The silica weight percent calculation utilizes Si to O bonding variability of silicate minerals, for example low (8–10 μm) absorption for mafic silicates (e.g., basalt) and high (8–10 μm) absorption for felsic silicates (e.g., granite) (see [72]).

$$\text{SiO}_2 = 56.20 - 271.09 \times \text{Log} \left[\frac{(\text{ASTe10} + \text{ASTe11} + \text{ASTe12})}{(3 \times \text{ASTe13})} \right] \quad (1)$$

where ASTe*n* corresponds to ASTER AST_05 surface emissivity product band number *n*.

Volcanic glacial study areas displayed lower supraglacial SiO₂ weight percent—58% for Mýradalsjökull supraglacial tephra and 56% for Whakapapa supraglacial tephra. Continental supraglacial debris displayed higher SiO₂ weight percentages—Khumbu supraglacial debris averaged 68% and Ngozumpa supraglacial debris 69%; Findelen supraglacial dust SiO₂ weight percent near the terminus was found to be 63% and Zmutt ablation area average SiO₂ weight percent of supraglacial debris was 71%. These TIR results are consistent with general mineralogy for the basaltic volcanic as well as continental supraglacial debris study regions, and generally agree well with the field collected surface glacier debris samples presented in Table 3. As noted in Hook *et al.* [72] continental or higher silicate TIR SiO₂ estimates tend to be slightly overestimated, and can be regionally fine tuned for greater accuracy (reported 2%–7% accuracy for regionally tuned TIR SiO₂ estimates). The difference between XRF and non-regionally tuned satellite TIR SiO₂ estimates was less than 1% variability in volcanic study regions, while continental estimates ranged from 7%–17%.

4.4. Use of Emissivity to Calculate Surface Temperature and Explore Mineral Influences

For each of the study regions, supraglacial temperatures were calculated in relation to amount and composition of debris (e.g., light, heavy debris cover, by mineral type) to explore mineral influences to glacier surface temperatures. Glacier surface temperatures for the various debris coverage and mineral types are listed in Table 6.

Table 6. Temperatures of bare ice vs. dust and debris covered ice in the four glacier study regions via use of the ASTER AST_08 Surface Kinetic Temperature data product, except the Vatnajökull values which were derived from ETM+ band 6 thermal data (denoted with “*”).

Region, Date	Glacier	Temp (°C)	Std. Dev.	No. pixels	$\Delta T_{debris} - T_{bareice}$ (°C)
Switzerland 7 July 2010	Gornergletscher, upper, slight dust	2.2	(0.5)	42	26.6
	Gornergletscher, lower, bare ice	3.5	(0.5)	23	
	Zmuttgletscher, heavy debris	28.8	(1.4)	40	
Nepal 29 November 2005	Khumbu, bare ice	−4.9	1.8	19	12.7
	Khumbu, heavy schistic debris	6.2	2.4	40	
	Khumbu, heavy granitic debris	7.8	2.1	14	
Iceland 25 August 2010	Vatnajökull*, light tephra	−3.3	(0.3)	6915	5.9
	Mýradalsjökull, light tephra	1.3	(0.3)	68	
	Mýradalsjökull, moderate tephra	1.8	(0.4)	119	
	Mýradalsjökull, heavy tephra	2.6	(0.5)	455	
New Zealand 9 January 2008	Mangachuehu, least tephra	3.2	0.5	14	15.2
	Mangatoetoenui, slight tephra	3.8	1.1	12	
	Whakapapa, heavy tephra	18.4	2.8	10	

ASTER AST_08 clear sky data acquired on 7 July 2010 was used to compare bare ice and slightly dust covered ice at Gorner glacier and heavily debris covered ice at nearby Zmutt glacier. Mean surface temperature of Gorner glacier bare cold ice in the ablation area was found to be 3.5 °C, and slightly dust covered ice in the accumulation area was found to be 2.2 °C. Nearby heavily debris covered Zmutt

glacier mean supraglacial temperature was found to be 28.8 °C, a difference of 25.3 or 26.6 °C between bare and slightly dust covered Gorner glacier ice, respectively.

Bare ice, schistic debris covered ice and granitic debris covered ice surface temperatures on Khumbu glacier in Nepal were analyzed from ASTER AST_08 data acquired 29 November 2005, in the late ablation season. The visually distinct schistic debris *vs.* the granitic debris (true color composite in Figure 2) were found to be over one degree apart: schistic debris 6.2 °C, and granitic debris 7.8 °C. Khumbu icefall bare ice was measured to be −4.9 °C, with the difference between bare ice and schistic debris 11.1 °C, and bare ice and granitic debris 12.7 °C.

In Iceland, heavily tephra covered Mýradalsjökull as well as lesser tephra covered Vatnajökull supraglacial temperatures were measured using ASTER AST_08 surface kinetic temperature and Landsat ETM+ derived surface temperature to spatially investigate both ice caps. ASTER data acquired on 25 August 2010 over Mýradalsjökull heavy tephra displayed an average surface temperature of 2.6 °C. Using Landsat ETM+ data also acquired on 25 August 2010, the least amount of supraglacial tephra over Vatnajökull was measured to be −3.3 °C. The difference between least tephra covered and most tephra covered ice in Iceland was measured to be 5.9 °C. Of note, no completely clear sky scenes of Iceland study area icecaps post-Eyjafjallajökull eruption were available at the time of publication. We speculate that total clear sky scenes in Iceland could yield even higher temperature differences between bare or lesser tephra covered and heavy supraglacial tephra coverage due to increased shortwave radiation. However, a total clear sky day Iceland scene may not result in marked differences, as partially cloudy AST_08 surface temperatures were compared with clear sky temperatures, and the results were found to be within 1 °C at each of the Gorner glacier and Zmutt glacier study sites.

Supraglacial tephra surface temperatures were inspected at Mt. Ruapehu area glaciers in New Zealand using ASTER AST_08 data collected 9 January 2008. The mean surface temperature of the least tephra covered glacier Mangaehuehu was 3.2 °C. The mean surface temperature of the slightly tephra covered glacier Mangatoetoeuui was 3.8 °C. The heaviest supraglacial tephra at Whakapapa glacier yielded a mean surface temperature of 18.4 °C. Thus, in the Mt. Ruapehu area glaciers, the difference between least supraglacial tephra and heavy supraglacial tephra was measured to be 15.2 °C.

From this study, continental supraglacial debris temperature variation within a scene was found to be from 12.7 to 26.6 °C, while volcanic supraglacial debris temperature variation was found to be from 5.9 to 15.2 °C. Continental supraglacial debris may have stronger potential to alter glacier surface temperature. Further supraglacial temperature variation analysis could prove promising toward radiative absorption glaciologic studies.

5. Conclusions

This study provided a fundamental step toward VNIR, SWIR and TIR satellite estimation of surface glacier dust and debris composition. Surface glacier dust, debris, ash and tephra sample mineralogy and trace elemental abundance results are given for the four distinct glacier regions. Analytical geochemical results were compared with satellite reflectance and emissivity derived surface glacier geochemical estimates, demonstrating that transition metal content can be determined by atmospherically corrected visible band absorption features, carbonate and silicate can be determined by SWIR reflectance and

silica content can be determined by ASTER TIR emissivity. ASTER TIR supraglacial silica content accuracies were within 1% in volcanic study regions and 7%–17% in continental study regions. Note, with regional tuning, continental supraglacial silica estimate accuracies are improved significantly. This study provided some of the first work toward supraglacial volcanic ash and tephra silica mapping, and given the high accuracies, this method may prove useful for characterizing volcanic eruptive impacts on land ice.

The VNIR-SWIR supraglacial dust and debris reflectance analysis suggested use of mapping thresholds for geochemical characterization. Volcanic ash and tephra, even at low concentrations, was differentiated by VNIR reflectance below 0.2 and SWIR reflectance below 0.1. Continental supraglacial debris often contains higher silica content, and in this study all continental debris was signaled by VNIR reflectance above 0.2 and SWIR reflectance above 0.1, often ranging up to 0.4 due to the high silica content. Automated mapping thresholds could be used to differentiate volcanic ash and tephra from continental dust and debris on land ice.

Emissivity-derived ablation season surface glacier temperatures demonstrated a significant range in temperature of differing supraglacial debris coverage in similar areas. Continental supraglacial debris temperature variations exceeded volcanic supraglacial debris temperature variations, with Switzerland supraglacial temperature variations at 25.3 and 26.6 °C, and Khumbu temperature variations at 11.1 and 12.7 °C vs. Iceland temperature variations at 5.9 °C and Ruapehu variations at 15.2 °C.

The sensors most amenable to quantitative determination of geologic composition are ASTER, MODIS and Hyperion. ASTER and Hyperion offer the highest spaceborne SWIR spectral resolution, while MODIS and ASTER offer the highest spaceborne TIR spectral resolution. The suite of Landsat sensors provide a means to qualitatively assess surface glacier geochemical composition via shortwave and thermal infrared image composites. Forthcoming Earth observation sensors include NASA's Landsat Data Continuity Mission (LDCM) and the European Space Agency's Sentinel-2. LDCM will collect similar Landsat heritage spectral and spatial resolution (plus an additional visible, NIR and 2 TIR bands at 15–100 m) and is expected to launch in early 2013. ESA's Sentinel-2 pair of VNIR-SWIR sensors (expected launch 2013) prove especially promising for global glacier monitoring, as they are designed to collect 13 VNIR-SWIR spectral bands, with 10–60 m spatial resolution on 2–5 day repeat temporal resolution. Such improved spatial and temporal global coverage address one of the primary limitations of current spectral glacier observations—simply the need for enhanced spatial, spectral and temporal coverage, as optical sensors rely on cloud-free atmosphere to collect reflective data.

Future work is recommended toward investigating supraglacial debris composition glacier variables, e.g., albedo, surface emissivity and temperature in relation to spatial geochemical supraglacial compositions. Investigation of topographic influences on supraglacial reflectance and emissivity could prove fruitful as supraglacial debris composition spatial variability can be related to elevation, aspect, slope and atmospheric influences. Atmospheric transport and mapping of particulate plumes may be enhanced by the methods presented in this study to map surface glacier geochemical composition and pinpoint ash, tephra, dust and debris provenance.

Acknowledgments

This work was funded by the University of Oslo, Department of Geosciences; the ESA GlobGlacier project (21088/07/I-EC) and the NASA Postdoctoral Program administered by Oak Ridge Associated Universities. The authors thank two anonymous reviewers and the editor for constructive feedback. We thank M. Zemp of the World Glacier Monitoring Service for logistic support toward Swiss Alps field work. We are grateful to glaciologists A. Barrueto and E. Rinne for one day each field support at Zmutt glacier. The authors thank R. Xie and B. L. Berg of the University of Oslo for assistance with XRD and XRF analysis.

References

1. Dyurgerov, M.; Meier, M. *Glaciers and the Changing Earth System: A 2004 Snapshot*; Occasional Paper 58; Institute of Arctic and Alpine Research, University of Colorado: Boulder, CO, USA, 2005; p. 117.
2. Thompson, L. Climate change: The evidence and our options. *Behav. Anal.* **2010**, *33*, 1153–1170.
3. Kang, S.; Wake, C.; Dahe, Q.; Mayewski, P.; Tandong, Y. Monsoon and dust signals recorded in Dasuopu glacier, Tibetan Plateau. *J. Glaciol.* **2000**, *46*, 222–226.
4. Fischer, H.; Siggaard-Andersen, M.L.; Ruth, U.; Röthlisberger, R.; Wolff, E. Glacial/interglacial changes in mineral dust and sea-salt records in polar ice cores: Sources, transport, and deposition. *Rev. Geophys.* **2007**, *45*, doi:10.1029/2005RG000192.
5. Thevenon, F.; Anselmetti, F.; Bernasconi, S.; Schwikowski, M. Mineral dust and elemental black carbon records from an Alpine ice core (Colle Gnifetti glacier) over the last millennium. *J. Geophys. Res.* **2009**, *114*, doi:10.1029/2008JD011490.
6. Kaspari, S.; Schwikowski, M.; Gysel, M.; Flanner, M.; Kang, S.; Hou, S.; Mayewski, P. Recent increase in black carbon concentrations from a Mt. Everest ice core spanning 1860–2000 AD. *Geophys. Res. Lett.* **2011**, *38*, doi:10.1029/2010GL046096.
7. Hansen, J.; Nazarenko, L. Soot climate forcing via snow and ice albedos. *Proc. Natl. Acad. Sci. USA* **2004**, *101*, 423–428.
8. Xu, B.; Cao, J.; Hansen, J.; Yao, T.; Joswila, D.R.; Wang, N.; Wu, G.; Wang, M.; Zhao, H.; Yang, W.; Liu, X.; He, J. Black soot and the survival of Tibetan glaciers. *Proc. Natl. Acad. Sci. USA* **2009**, *106*, 22114–22118.
9. Oerlemans, J.; Giesen, R.; van den Broeke, M. Retreating alpine glaciers: Increased melt rates due to accumulation of dust (Vadret da Morteratsch, Switzerland). *J. Glaciol.* **2009**, *55*, 729–736.
10. Kok, J.F. A scaling theory for the size distribution of emitted dust aerosols suggests climate models underestimate the size of the global dust cycle. *Proc. Natl. Acad. Sci. USA* **2011**, *108*, 1016–1021.
11. McKendry, I.; Strawbridge, K.; O'Neill, N.; Macdonald, A.; Liu, P.; Leaitch, W.; Anlauf, K.; Jaegle, L.; Fairlie, T.; Westphal, D. Trans-Pacific transport of Saharan dust to western North America: A case study. *J. Geophys. Res.* **2007**, *112*, doi:10.1029/2006JD007129.
12. Uno, I.; Eguchi, K.; Yumimoto, K.; Takemura, T.; Shimizu, A.; Uematsu, M.; Liu, Z.; Wang, Z.; Hara, Y.; Sugimoto, N. Asian dust transported one full circuit around the globe. *Nat. Geosci.* **2009**, *2*, 557–560.

13. Gangale, G.; Prata, A.; Clarisse, L. The infrared spectral signature of volcanic ash determined from high-spectral resolution satellite measurements. *Remote Sens. Environ.* **2010**, *114*, 414–425.
14. Brenning, A. The Impact of Mining on Rock Glaciers and Glaciers: Examples from Central Chile. In *Darkening Peaks: Glacier Retreat, Science and Society*; Orlove, B., Wiegandt, E., Luckman, B., Eds.; University of California Press: Berkeley, CA, USA, 2008; Chapter 14, pp. 196–205.
15. Crusius, J.; Schroth, A.; Gasso, S.; Moy, C.; Levy, R.; Gatica, M. Glacial flour dust storms in the Gulf of Alaska: Hydrologic and meteorological controls and their importance as a source of bioavailable iron. *Geophys. Res. Lett.* **2011**, *38*, doi:10.1029/2010GL046573 .
16. Gleeson, D.F.; Pappalardo, R.T.; Grasby, S.E.; Anderson, M.S.; Beauchamp, B.; Castaño, R.; Chien, S.A.; Doggett, T.; Mandrake, L.; Wagstaff, K.L. Characterization of a sulfur-rich Arctic spring site and field analog to Europa using hyperspectral data. *Remote Sens. Environ.* **2010**, *114*, 1297–1311.
17. Kääb, A.; Paul, F.; Maisch, M.; Hoelzle, M.; Haeberli, W. The new remote-sensing-derived Swiss glacier inventory: II. First results. *Ann. Glaciol.* **2002**, *34*, 362–366.
18. Schneider, C.; Schnirch, M.; Acuña, C.; Casassa, G.; Kilian, R. Glacier inventory of the Gran Campo Nevado Ice Cap in the Southern Andes and glacier changes observed during recent decades. *Glob. Planet. Chang.* **2007**, *59*, 87–100.
19. Bolch, T.; Menounos, B.; Wheate, R. Landsat-based inventory of glaciers in western Canada, 1985–2005. *Remote Sens. Environ.* **2010**, *114*, 127–137.
20. Raup, B.; Racoviteanu, A.; Khalsa, S.; Helm, C.; Armstrong, R.; Arnaud, Y. The GLIMS geospatial glacier database: A new tool for studying glacier change. *Glob. Planet. Chang.* **2007**, *56*, 101–110.
21. Paul, F.; Barry, R.; Cogley, J.; Frey, H.; Haeberli, W.; Ohmura, A.; Ommanney, C.; Raup, B.; Rivera, A.; Zemp, M. Recommendations for the compilation of glacier inventory data from digital sources. *Ann. Glaciol.* **2009**, *50*, 119–126.
22. Escher, A.; Beaumont, C. Formation, burial and exhumation of basement nappes at crustal scale: A geometric model based on the Western Swiss-Italian Alps. *J. Struc. Geol.* **1997**, *19*, 955–974.
23. Reid, H. The mechanics of glaciers. I. *J. Geol.* **1896**, *4*, 912–928.
24. Machguth, H.; Paul, F.; Hoelzle, M.; Haeberli, W. Distributed glacier mass-balance modelling as an important component of modern multi-level glacier monitoring. *Ann. Glaciol.* **2006**, *43*, 335–343.
25. Wei, Z. Chemical Evolution at Surface Condition in the Zermatt-Saas Area (Swiss Alps): A Geo-Hydrochemistry Study on Surface Water-Rock Interaction. Ph.D. Thesis, Universität Freiburg, Freiburg, Germany, 2010.
26. Gruber, S.; Hoelzle, M. Statistical modelling of mountain permafrost distribution: Local calibration and incorporation of remotely sensed data. *Permafr. Periglac. Process.* **2001**, *12*, 69–77.
27. Tartari, G.; Verza, G.; Bertolami, L. Meteorological data at the Pyramid Observatory Laboratory (Khumbu Valley, Sagarmatha National Park, Nepal). *Mem. Ist. Ital. Idrobiol.* **1998**, *57*, 23–40.
28. Hambrey, M.; Quincey, D.; Glasser, N.; Reynolds, J.; Richardson, S.; Clemmens, S. Sedimentological, geomorphological and dynamic context of debris-mantled glaciers, Mount Everest (Sagarmatha) region, Nepal. *Quat. Sci. Rev.* **2008**, *27*, 2361–2389.

29. de Woul, M.; Hock, R.; Braun, M.; Thorsteinsson, T.; Jóhannesson, T.; Halldórsdóttir, S. Firn layer impact on glacial runoff: A case study at Hofsjökull, Iceland. *Hydrol. Process.* **2006**, *20*, 2171–2185.
30. Gudmundsson, S.; Magnússon, E.; Björnsson, H.; Pálsson, F.; Gudmundsson, M.; Högnadóttir, D.; Berthier, E.; Jóhannesson, T.; Sigurdsson, O.; Dorsteinsson, D.; Dall, J. Volume and Mass Balance Changes of Ice Caps in Iceland Deduced from Elevation Data and *in situ* Mass Balance Observations. In *Proceedings of SPIRIT Workshop*, Toulouse, France, 29–30 April 2010.
31. Searle, M.; Simpson, R.; Law, R.; Parrish, R.; Waters, D. The structural geometry, metamorphic and magmatic evolution of the Everest massif, High Himalaya of Nepal-South Tibet. *J. Geol. Soc.* **2003**, *160*, 345–366.
32. Scherler, D.; Bookhagen, B.; Strecker, M. Spatially variable response of Himalayan glaciers to climate change affected by debris cover. *Nat. Geosci.* **2011**, *4*, 156–159.
33. Luo, R.; Cao, J.; Liu, G.; Cui, Z. Characteristics of the subglacially-formed debris-rich chemical deposits and related subglacial processes of Qiangyong Glacier, Tibet. *J. Geogr. Sci.* **2003**, *13*, 455–462.
34. De Ruyter de Wildt, M.; Oerlemans, J.; Björnsson, H. A method for monitoring glacier mass balance using satellite albedo measurements: Application to Vatnajökull, Iceland. *J. Glaciol.* **2002**, *48*, 267–278.
35. Gudmundsson, A. Dynamics of volcanic systems in Iceland: Example of tectonism and volcanism at juxtaposed hot spot and mid-ocean ridge systems. *Ann. Rev. Earth Planet. Sci.* **2000**, *28*, 107–140.
36. Thordarson, T.; Larsen, G. Volcanism in Iceland in historical time: Volcano types, eruption styles and eruptive history. *J. Geodyn.* **2007**, *43*, 118–152.
37. Haflidason, H.; Eiriksson, J.; Kreveld, S. The tephrochronology of Iceland and the North Atlantic region during the Middle and Late Quaternary: A review. *J. Quat. Sci.* **2000**, *15*, 3–22.
38. Dibble, R. Volcanic Seismology and Accompanying Activity of Ruapehu Volcano, New Zealand. In *Physical Volcanology*; Elsevier: New York, NY, USA, 1974; pp. 49–85.
39. Hackett, W.; Houghton, B. A facies model for a quaternary andesitic composite volcano: Ruapehu, New Zealand. *Bull. Volcanol.* **1989**, *51*, 51–68.
40. Chinn, T. Distribution of the glacial water resources of New Zealand. *J. Hydrol. (NZ)* **2001**, *40*, 139–187.
41. NZDOC. Tongariro Parkmap 273-04. In *New Zealand Department of Conservation*; 6th ed.; GeoSmart: North Shore, New Zealand, 2004.
42. Hurst, A.; Bibby, H.; Scott, B.; McGuinness, M. The heat source of Ruapehu crater lake: Deductions from the energy and mass balances. *J. Volcanol. Geotherm. Res.* **1991**, *46*, 1–20.
43. Werner, C.; Christenson, B.; Hagerty, M.; Britten, K. Variability of volcanic gas emissions during a crater lake heating cycle at Ruapehu Volcano, New Zealand. *J. Volcanol. Geotherm. Res.* **2006**, *154*, 291–302.
44. Williams, K. *Volcanoes of the South Wind: A Field Guide to the Volcanoes and Landscape of Tongariro National Park*; Tongariro Natural History: Turangi, New Zealand, 2001; p. 146.

45. Keys, H. Lahars of Ruapehu Volcano, New Zealand: Risk mitigation. *Ann. Glaciol.* **2007**, *45*, 155–162.
46. Keys, H.; Green, P. Ruapehu Lahar New Zealand 18 March 2007: Lessons for hazard assessment and risk mitigation 1995–2007. *J. Disaster Res.* **2008**, *3*, 284–296.
47. Christenson, B.; Reyes, A.; Young, R.; Moebis, A.; Sherburn, S.; Cole-Baker, J.; Britten, K. Cyclic processes and factors leading to phreatic eruption events: Insights from the 25 September 2007 eruption through Ruapehu Crater Lake, New Zealand. *J. Volcanol. Geotherm. Res.* **2010**, *191*, 15–32.
48. Kilgour, G.; Manville, V.; Pasqua, F.D.; Graettinger, A.; Hodgson, K.; Jolly, G. The 25 September 2007 eruption of Mount Ruapehu, New Zealand: Directed ballistics, surtseyan jets, and ice-slurry lahars. *J. Volcanol. Geotherm. Res.* **2010**, *191*, 1–14.
49. Manville, V.; Hodgson, K.; Houghton, B.; Keys, H.; White, J. Tephra, snow and water: Complex sedimentary responses at an active snow-capped stratovolcano, Ruapehu, New Zealand. *Bull. Volcanol.* **2000**, *62*, 278–293.
50. Casey, K.; Kääh, A.; Benn, D. Geochemical characterization of supraglacial debris via *in situ* and optical remote sensing methods: A case study in the Khumbu Himalaya, Nepal. *Cryosphere* **2012**, *6*, 85–100.
51. Gislason, S.; Hassenkam, T.; Nedel, S.; Bovet, N.; Eiríksdóttir, E.; Alfredsson, H.; Hem, C.; Balogh, Z.; Dideriksen, K.; Oskarsson, N.; Sigfusson, B.; Larsen, G.; Stipp, S. Characterization of Eyjafjallajökull volcanic ash particles and a protocol for rapid risk assessment. *Proc. Natl. Acad. Sci.* **2011**, *108*, 7307–7312.
52. Clark, R.; Roush, T. Reflectance spectroscopy: Quantitative analysis techniques for remote sensing applications. *J. Geophys. Res.* **1984**, *89*, 6329–6340.
53. Hook, S.J.; Gabell, A.; Green, A.; Kealy, P. A comparison of techniques for extracting emissivity information from thermal infrared data for geologic studies. *Remote Sens. Environ.* **1992**, *42*, 123–135.
54. Box, J.; Fettweis, X.; Stroeve, J.; Tedesco, M.; Hall, D.; Steffen, K. Greenland ice sheet albedo feedback: Thermodynamics and atmospheric drivers. *Cryosphere* **2012**, *6*, 821–839.
55. Iwasaki, A.; Tonooka, H. Validation of a crosstalk correction algorithm for ASTER/SWIR. *IEEE Trans. Geosci. Remote Sens.* **2005**, *43*, 2747–2751.
56. Markham, B.; Barker, J. *Landsat MSS and TM Post-Calibration Dynamic Ranges, Exoatmospheric Reflectances and at-Satellite Temperatures*; EOSAT Landsat Tech. Notes 1; NASA/GSFC: Greenbelt, MD, USA, 1986, pp. 3–8.
57. Barry, P. *EO-1 Hyperion Science Data User's Guide, Level 1_B*; NASA Tech. Doc.; TRW: Redondo Beach, CA, USA, 2001; p. 52.
58. Watanabe, H.; Matsuo, K. Rock type classification by multi-band TIR of ASTER. *Geosci. J.* **2003**, *7*, 347–358.
59. Barsi, J.; Schott, J.; Palluconi, F.; Hook, S. Validation of a web-based atmospheric correction tool for single thermal band instruments. *Proc. SPIE* **2005**, 5882, 58820E–58820E-7.

60. Hall, D.; Box, J.; Casey, K.; Hook, S.; Shuman, C.; Steffen, K. Comparison of satellite-derived and in-situ observations of ice and snow surface temperatures over Greenland. *Remote Sens. Environ.* **2008**, *112*, 3739–3749.
61. Zeng, Q.; Cao, M.; Feng, X.; Liang, F.; Chen, X.; Sheng, W. A Study of Spectral Reflection Characteristics for Snow, Ice and Water in the North of China. In *Hydrological Applications of Remote Sensing and Remote Data Transmission: Proceedings of the Hamburg Symposium*; Goodison, B., Ed.; IAHS Publ. No. 145; IAHS: Oxford, UK, 1985; pp. 451–462.
62. Price, J. Comparing MODIS and ETM+ data for regional and global land classification. *Remote Sens. Environ.* **2003**, *86*, 491–499.
63. Gupta, R.P. *Remote Sensing Geology*, 2nd ed.; Springer: Berlin/Heidelberg, Germany, 2003; p. 655.
64. Kääb, A. *Remote Sensing of Mountain Glaciers and Permafrost Creep*; Volume 48, Schriftenreihe Physische Geographie: Zurich, Switzerland, 2005; p. 266.
65. Vincent, R.; Thomson, F. Rock-type discrimination from ratioed infrared scanner images of Pisgah Crater, California. *Science* **1972**, *175*, 986–988.
66. Ninomiya, Y. Rock type mapping with indices defined for multispectral thermal infrared ASTER data: Case studies. *Proc. SPIE* **2003**, doi: 10.1117/12.462358.
67. Kruse, F.; Boardman, J.; Huntington, J. Comparison of airborne hyperspectral data and EO-1 Hyperion for mineral mapping. *IEEE Trans. Geosci. Remote Sens.* **2003**, *41*, 1388–1400.
68. Chan, J.C.W.; Ophem, J.V.; Huybrechts, P. Estimation of Accumulation Area Ratio of a Glacier from Multi-Temporal Satellite Images Using Spectral Unmixing. In *Proceedings of the IEEE Geoscience and Remote Sensing Symposium*, Cape Town, South Africa, 12–17 July 2009; Volume 2, II–606–II–609.
69. Painter, T.; Rittger, K.; McKenzie, C.; Slaughter, P.; Davis, R.; Dozier, J. Retrieval of subpixel snow covered are, grain size, and albedo from MODIS. *Remote Sens. Environ.* **2009**, *113*, 868–879.
70. Clark, R.; Lucey, P. Spectral properties of ice-particulate mixtures and implications for remote sensing 1. Intimate mixtures. *J. Geophys. Res.* **1984**, *89*, 6341–6348.
71. Mars, J.; Rowan, L. ASTER spectral analysis and lithologic mapping of Khanneshin carbonatite volcano, Afghanistan. *Geosphere* **2011**, *7*, 276–289.
72. Hook, S.; Dmochowski, J.; Howard, K.; Rowan, L.; Karlstrom, K.; Stock, J. Mapping variations in weight percent silica measured from multispectral thermal infrared imagery—Examples from the Hiller Mountains, Nevada, USA and Tres Virgenes-La Reforma, Baja California Sur, Mexico. *Remote Sens. Environ.* **2005**, *95*, 273–289.